Geo-information Science and Remote Sensing

Thesis Report GIRS-2018-46

The use of Markov Random Field for tropical deforestation detection in dense C-band SAR time-series.

Jorn van der Ent

October 29, 2018

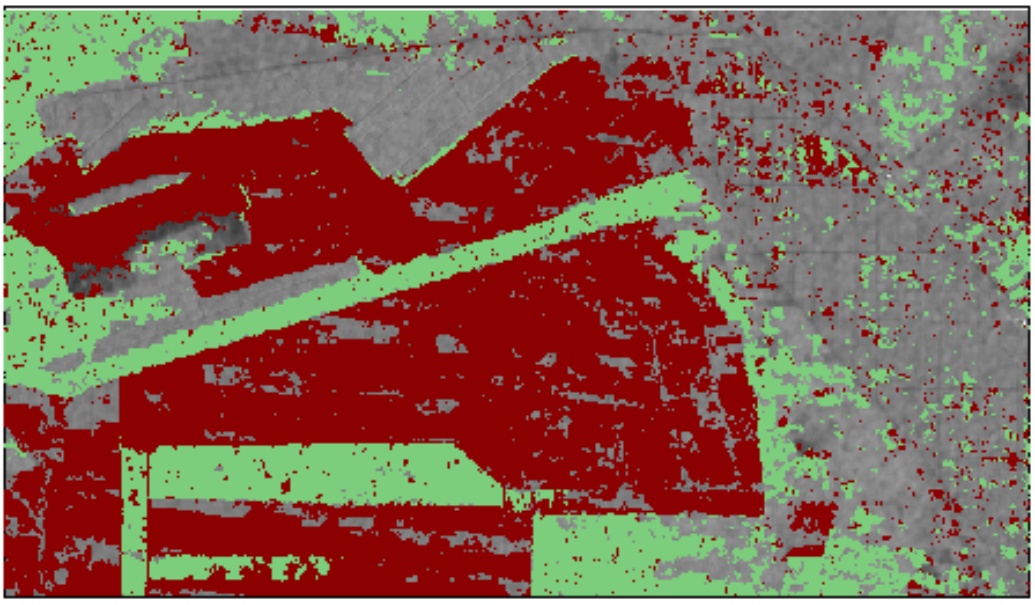

WAGENINGEN
UNIVERSITY & RESEARCH

The use of Markov Random Field for tropical deforestation detection in dense C-band SAR time-series.

Jorn van der Ent

Registration number 92 03 11 226 120

Supervisors:

Dr. Johannes Reiche
Dr. Devis Tuia

A thesis submitted in partial fulfilment of the degree of Master of Science
at Wageningen University and Research Centre,
The Netherlands.

October 29, 2018
Wageningen, The Netherlands

Thesis code number: GRS-80436
Thesis Report: GIRS-2018-46
Wageningen University and Research Centre
Laboratory of Geo-Information Science and Remote Sensing

Abstract

Tropical forest have been increasingly threatened and stakeholders need accurate information to act. This thesis used MRF deforestation detection in C-band SAR data. With MRF, spatial and temporal context was used to improve classification accuracy. The SAR data was used for a first rough classification, after which a spatial, temporal or spatial-temporal MRF was applied to improve the classification. This resulted in an estimated user's accuracy of 63%, an producer's accuracy of 75% and an overall accuracy of 97%. The improvement of spatial classification accuracy had a trade-off with the temporal accuracy as the mean time-lag increased to 8 days on average. Data acquired during 2015 and 2016 over central Sumatra has been used for a proof-of-concept demonstration showing deforestation rates of 7.1% and 7.4% respectively.

Contents

List of Figures

List of Tables

List of Abbreviations

ALOS	**A**dvanced **L**and **O**bservation **S**atellite
ESA	**E**uropean **S**pace **A**gency
F	**F**orest
ICM	**I**terated **C**onditional **M**ode
LCT	**L**and **C**over **T**rajectory
LULC	**L**and-**U**se and **L**and-**C**over
MRF	**M**arkov **R**andom **F**ield
MTL	**M**ean **T**ime-**L**ag
NF	**N**on-**F**orest
NRT	**N**ear-**R**eal-**T**ime
OA	**O**veral **A**ccuracy
PA	**P**roducer **A**ccuracy
PALSAR	**P**hased **A**rray type **L**-band **S**ynthetic **A**perture **R**adar
PoI	**P**ixel **o**f **I**nterest
REDD	**R**educed **D**eforestation and **D**egradation
RF	**R**andom **F**orest
SAR	**S**ynthetic **A**perture **R**adar
S-MRF	**S**patial **M**arkov **R**andom **F**ield
ST-MRF	**S**pace-**T**ime **M**arkov **R**andom **F**ield
T-MRF	**T**emporal **M**arkov **R**andom **F**ield
UA	**U**ser **A**ccuracy
UNFCCC	**U**nited **N**ations **F**ramework **C**onvention on **C**limate **C**hange
VH	**V**ertical-**H**orizontal polarization
VV	**V**ertical-**V**ertical polarization

List of Symbols

θ	threshold
λ_{unary}	Unary weight
$\lambda_{spatial}$	Spatial weight
$\lambda_{temporal}$	Temporal weight
γ^0	Backscatter
$P(nf)$	Non-Forest Probability

1 Introduction

Tropical rainforests have become increasingly threatened by both legal and illegal deforestation, forest degradation, and agricultural expansion (Achard, 2002). Forest cover change affects the Earth's ecosystem services far beyond the boundaries of the original region, and has influenced the climate directly at local and even regional scales (Foley, 2005; Vitousek et al., 1997; Myers, 1988; Santilli et al., 2005). Besides the climatic consequences, illegal logging activities caused financial losses (Li et al., 2008; Turner et al., 2008; Brack, 2003).
The United Nations Framework Convention on Climate Change (UNFCCC) has been facilitating large-scale forest monitoring for Reduced Deforestation and Degradation (REDD) since 1997 (Holloway and Giandomenico, 2009). In order to obtain detailed knowledge and information on forests, a Near-Real-Time (NRT) monitoring system is often used.

NRT monitoring systems for forests rely heavily on aerial photography or satellite imagery (Cohen et al., 1996; Asner, 2009; Fuller, 2006; Lynch et al., 2013). The satellites provide the only data stream capable of repetitive observations of forest areas (Lynch et al., 2013; Hansen et al., 2013). Therefore, time-series data produced by satellites are used as the primary data source for deforestation detection in a NRT monitoring system (Assunção, Gandour, and Rocha, 2013; Hansen et al., 2008; Li et al., 2011; Liu and Cai, 2012; Reiche et al., 2015a; Ryan et al., 2012). However, satellites have a revisit time, the time between 2 acquisitions at a certain location. In between 2 acquisitions an area could be deforested, which will not be visible until the next satellite visit. Therefore, there is a time-delay between the moment deforestation occurs and when it appears on a satellite image. This time-delay prevents a satellite-based system from being real-time. Therefore these systems are referred to as NRT monitoring systems.

Satellites equipped with a Synthetic Aperture Radar (SAR) system have a high potential in tropical regions (Lynch et al., 2013). These satellites send pulses to the Earth's surface, and the echo of each pulse (backscatter) is recorded. Due to the presence of clouds throughout the year, multi-spectral remote sensing data is limited in tropical regions (Müller et al., 2015; Rufin et al., 2015). SAR is able to penetrate the clouds, and interacts with the objects on the ground. However, due to strong backscatter variations (speckle) in individual images, SAR data is limited compared to multi-spectral data (Kumar and Patnaik, 2013; Goodman, 1976). Nonetheless, various studies have highlighted the potential of SAR data for land-use and land-cover (LULC) mapping (Kasischke, Melack, and Dobson, 1997; Qi et al., 2012; Uhlmann and Kiranyaz, 2014; Almeida-Filho et al., 2009) and change detection (Reiche et al., 2015b; Reiche et al., 2013; Trier and Salberg, 2011; Rahman and Sumantyo, 2010).
The recently launched Sentinel-1 mission shows potential for a NRT monitoring system. Sentinel-1 has many more observations per year in comparison to other satellites, like ALOS PALSAR. Sentinel-1 provides C-band images in VV and VH polarizations. The increase in observations could contribute to a more reliable NRT

monitoring system (Reiche et al., 2013; Reiche et al., 2016).

In order to detect deforestation from Sentinel-1 SAR images, individual pixels have to be transformed from backscatter to LULC classes. Many statistical learning frameworks are available for this transformation. Traditional frameworks such as minimum distance and maximum likelihood have been widely used (Lu and Weng, 2007; Lu et al., 2004). In recent years, more advanced approaches, like the Random Forest model (RF) (Breiman, 2001), have been gaining popularity in a variety of disciplines (Bengio, Courville, and Vincent, 2013), including remote sensing (Coulston et al., 2012; Vuolo et al., 2013; Du et al., 2015; Belgiu and Drăgu, 2016). With RF, data from multiple sources can be easily added. These sources could include VV & VH SAR polarization, multi-spectral imagery, hyper-spectral airborne data, weather data, and geographic data such as elevation and slope (Gislason, Benediktsson, and Sveinsson, 2006). This has resulted in RF outperforming traditional methods in a range of studies (Schindler, 2012; Gislason, Benediktsson, and Sveinsson, 2006; Müller et al., 2015; Waske and Braun, 2009).
However, both modern and traditional methods are affected by speckle in SAR images (Goodman, 1976). To account for speckle, one might look into the first law of geography, first described by Tobler (1970): "Everything is related to everything else, but near things are more related than distant things". To some extent this is applicable to SAR images. Spatial context could be used in order to reduce the effect of speckle, which forms the basis of many speckle-filters (Sheng and Xia, 1996). Next to spatial context, temporal context could also be included. Clearly recognizable temporal signatures caused by land management, crop type and the seasonal cycle have shown to improve classification (Blaes, Vanhalle, and Defourny, 2005; McNairn et al., 2009; Coppin et al., 2004; Hagensieker et al., 2017; Verbesselt et al., 2010; Reiche et al., 2015a).

For a NRT monitoring system to include both spatial and temporal relations, the Markov random fields (MRF's) could be used as an effective and theoretically well-established mathematical tool. MRF's allows for the integration of contextual information into the classification scheme (Melgani and Serpico, 2003; Moser, Serpico, and Benediktsson, 2013; Moser and Serpico, 2013; Liu, Kelly, and Gong, 2006). Often, temporal relations are modeled with transition matrices, e.g. probabilities of class changing to a certain other class (Hagensieker et al., 2017; Fu, Guo, and Zhou, 2009; Cai et al., 2014; Wehmann and Liu, 2015; Liu et al., 2008), or a second order neighborhood (8 surrounding pixels) system (Hagensieker et al., 2017; Wehmann and Liu, 2015; Liu, Kelly, and Gong, 2006; Melgani and Serpico, 2003; Liu and Cai, 2012). MRFs model the spatial and temporal context in an energy function (the term originates from thermodynamics). The spatial and temporal contexts are described in terms in this energy function. The costs of different LULC classes are compared and the class of which the energy cost is the lowest, will be assigned.

2 Research Objectives

The aim of this study was to adapt MRF for time-series deforestation detection in tropical regions. Different approaches were explored, i.e, using spatial and/or temporal context. The inclusion of spatial and temporal context was studied separately, each dependent on certain parameters. After that, the spatial en temporal contexts were combined. For the spatial MRF (S-MRF), the number of iterations and division of weights was varied. In the temporal MRF (T-MRF), the number of temporal neighbors and division of weights was varied. The optimal number of iterations and temporal neighbors found in the separate S-MRF and T-MRF studies, were used in a combined space-time MRF (ST-MRF), where only the division of weights was varied. Eventually the best method, S-MRF, T-MRF or ST-MRF was used for a practical showcase, in which the deforestation rate in the Riau province, Sumatra, Indonesia was determined.

This translates into the following research questions:

1. What improvement is observed when spatial and/or temporal information is added to time-series deforestation detection?
2. What MRF approach yields optimal results?
   (a) What number of iteration is best for a S-MRF?
   (b) What number of temporal neighbors is best for modeling temporal information?
   (c) What weight division is best for a ST-MRF?
3. What is the deforestation rate for the Riau province, Sumatra, Indonesia in 2015 and 2016?

3 Data

3.1 Study Area

This study was tested on data from the Riau province on the island of Sumatra, Indonesia (Figure 3.1. Figure 3.2 shows SAR images of the area. The area is mostly covered by plantations. Other land-cover types are urban and protected forest areas.

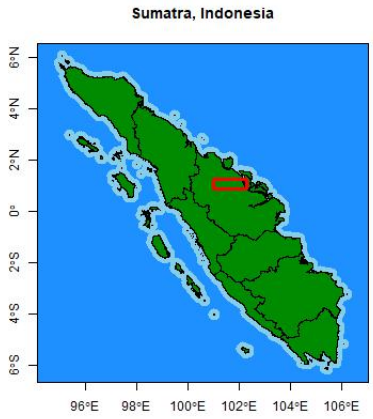

FIGURE 3.1: Location of the study area, a part of the province of Riau in Sumatra, Indonesia.

3.2 Datasets

Multi-temporal C-band SAR data was obtained from ESA's Sentinel-1 satellite in the period from 22 October 2014 to 9 February 2017. The time-series consists of 83 images in VV and VH polarization with an average revisit time of 10 days. Figure 3.2 shows the first images of the time-series, with manually selected testing sites. The VV and VH datasets were pre-processed and provided by Dr. J. Reiche of the Laboratory of Geo-information Science and Remote Sensing at Wageningen University. The individual VV and VH images were stacked and ordered chronologically. The images display return values γ^0 in dB (backscatter), and were projected with the WGS 84 reference coordinate system.

A forest mask, developed by Hansen et al. (2013), was used in determining the deforestation rate of the Riau area (Figure 3.3).

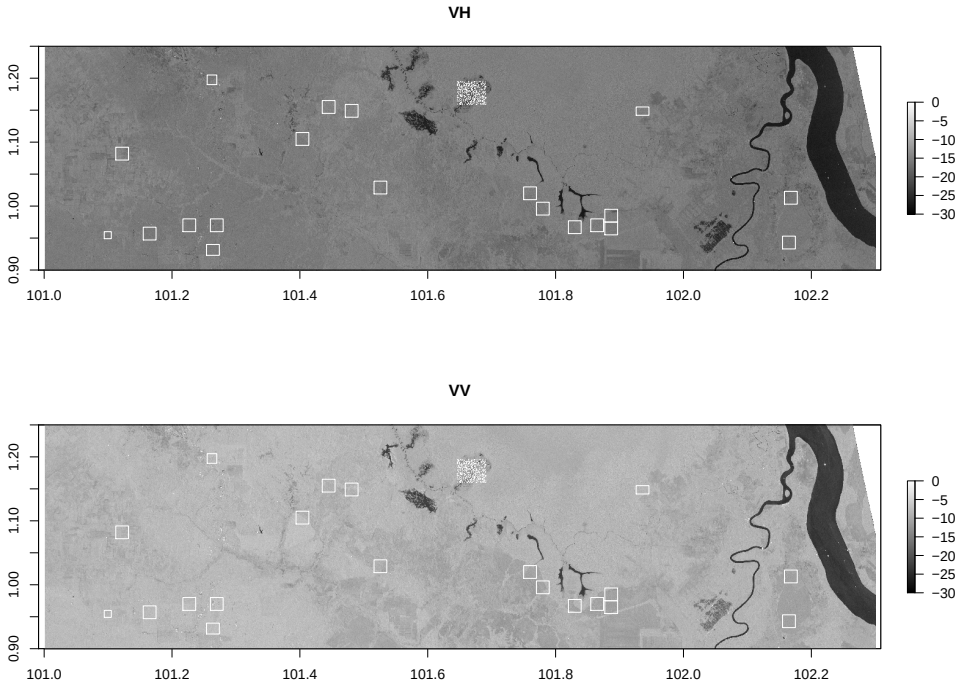

FIGURE 3.2: The VH and VV image acquired 22 October 2014 of the study area, with manually selected training sites.

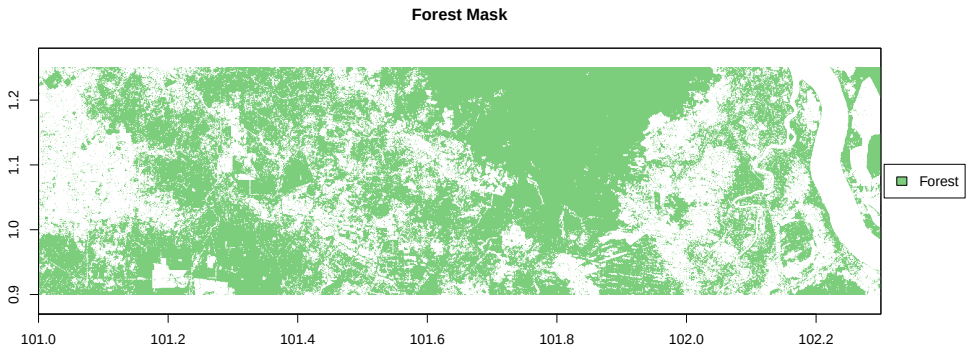

FIGURE 3.3: Forest mask as developed by (Hansen et al., 2013).

4 Methodology

4.1 Overview

Sentinel-1 C-band data was acquired in VV and VH polarization. The VV and VH images were transformed into non-forest probabilities by a RF model. The RF model was trained from data distributed over Riau (Figure 3.2). A spatial (S-MRF) and temporal MRF (T-MRF) were developed and studied separately, before being combined in a space-time MRF (ST-MRF) (Figure 4.1).

The S-MRF was used to study the effects of iterations and weight devision. Instead of using spatial neighbors, the T-MRF used temporal neighbors. The number of temporal neighbors was varied and the effect on classification accuracy was monitored.

Testing and developing the spatial en temporal MRF separately allowed for educated decisions on developing an ST-MRF. The effect of the weight distributions in the ST-MRF was measured. The best method, S-MRF, T-MRF or ST-MRF, with the best parameters was then used to determine the deforestation rate in Riau during the monitoring period.

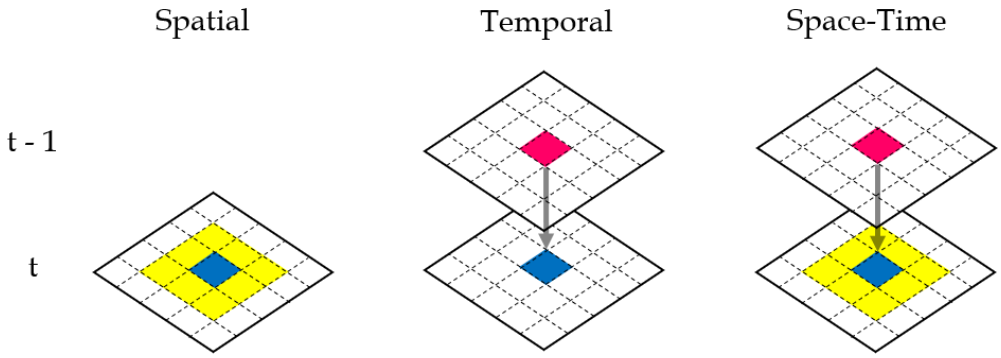

FIGURE 4.1: Development stages of the space-time MRF. Temporal neighborhood (red) and spatial neighbors (yellow) of a pixel of interest (blue).

4.2 Sampling Scheme

In order to develop and test the proposed method, training and validation data were collected. 20 Training sites were selected in the study area, shown in Figure 3.2. The sites were distributed across the area, in order to create variability in the data. All sites contained deforested and stable forest areas, and had an approximate size of 100 by 100 pixels.

From each of the 20 sites, 25 random samples were taken for training the model, and another 25 random samples were taken for validation (Figure 4.2). So 500 samples were used for training purposes, and 500 other samples for the validation. Each sample was a location of which a time-series of 83 images was available. To track the sample through time, Figure 4.3 was constructed. The sample in the figure was deforested during the observation period. The moment at which the deforestation event is visible for the first time, is referred to as the reference date.

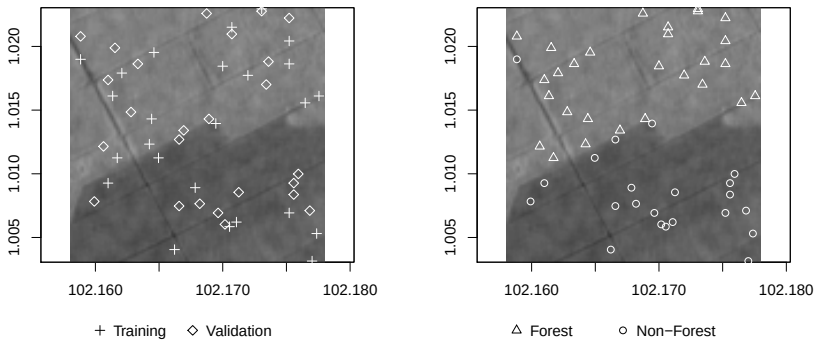

FIGURE 4.2: Randomly selected training & validation samples and their forest or non-forest classification.

The time-series signal in Figure 4.3 shows a deforestation event. After a deforestation event, the vegetation starts to regrow. As the area would regrow, the signal would recover to its original state. During this period of regrowth it is difficult to assign a forest or non-forest classification (Joshi et al., 2015; Mermoz and Le Toan, 2016; Cohen, Yang, and Kennedy, 2010), which interferes with the validation of the model. Because this study focuses on the detection of the deforestation event, more recent acquired data (10 time-steps after the reference date) was not used in estimating the accuracies of the proposed method.

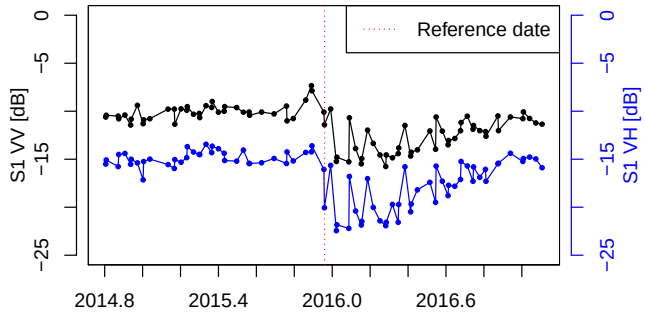

FIGURE 4.3: Example of the reference date with a Sentinel-1 VH&VV single pixel time-series of a pixel which was deforested.

4.3 Random Forest

Before applying the MRF, the VV & VH data stacks were transformed from backscatter into non-forest probabilities ($P(nf)$). A RF classifier was used for this transformation (Liaw and Wiener, 2002). The RF model was trained with 500 random samples, see Section 4.2, of which 240 were deforested and 260 remained forest throughout the observation period. For the deforested samples, VV&VH data was extracted from the time-series at the reference date. A random chosen observation date was used to collect data for the forest samples. After training, the RF model assigned a probability of non-forest, knowing the VV & VH for each pixel (Figure 4.4).
$P(nf)$ Was used as an input for the MRFs. The expected improvements by the MRF were compared with the performance of the RF classification output.

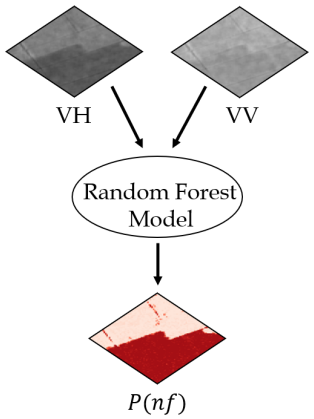

FIGURE 4.4: Transformation of VV & VH to $P(nf)$.

4.4 Markov Random Field

The main method in this study was the MRF. The spatial and temporal contexts were each represented by a pairwise term in the energy function. Another term, referred to as the unary term, was the $P(nf)$. This study considered 2 classes, forest (F) and non-forest (NF). The energy-costs of assigning a class were calculated with Equation 4.1, in which the class with minimum energy, Equation 4.2, was assigned.

$$E_{F \vee NF} = -\log^{10}(unary + spatial + temporal) \tag{4.1}$$

$$class = min(E_F \vee E_{NF}) \tag{4.2}$$

The values of the unary and pairwise terms were on a scale from 0 to 1. In addition, the terms had weights (λ) assigned so that Equation 4.1 becomes Equation 4.3, where the sum of the weights was equal to 1, e.g. $\lambda_{unary} + \lambda_{spatial} + \lambda_{temporal} = 1$

$$E_{F \vee NF} = -\log^{10}(\lambda_{unary} \times unary + \lambda_{spatial} \times spatial + \lambda_{temporal} \times temporal) \tag{4.3}$$

4.4.1 Spatial Term

In constructing the spatial term of the MRF, the $P(nf)$ was used. The $P(nf)$ was converted to classes using threshold θ (Figure 4.5a), which θ had a value between 0

and 1. All pixels with a $P(nf)$ equal to or above θ were classified as NF. The pixels with values below θ were classified as F. In this study, a θ of 0.5 was used, which resulted in the classification shown in Figure 4.5b. Now, the neighborhood of the pixel of interest (PoI) will further influence the classification. The sum of the NF pixels in the 2^d order neighborhood (5 pixels), including the PoI (0 pixel), was divided by the total number of pixels (9 pixels). This results in a normalized value for the spatial term, again on the same scale as $P(nf)$. The result of this example is shown in Figure 4.5c.

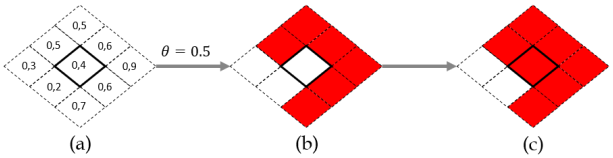

FIGURE 4.5: Conversion of $P(nf)$ (a) to a classification map (b). Using both the original $P(nf) = 0.4$ and the contribution from the neighbors (5/9), the PoI is eventually attributed to the NF class (c).

In this example the PoI has changed from F to NF. However, the same approach have been applied on the neighboring pixels. This might change the classification of the neighbors, which impacts the energy function. The calculation can be done again for this new situation. Therefore the S-MRF was used iteratively. The iterated conditional mode (ICM), which was used here, assumes that the final iteration, a stable situation, would be the best solution as it has the minimum energy. However, this is correct locally (the neighborhood) and not globally (the image). In addition, the iterations are computationally expensive (Moser and Serpico, 2013; Solberg, Taxt, and Jain, 1996; Besag, 1986; Wehmann and Liu, 2015), while increase in classification accuracy might be little. Because of this trade-off, the impact of each iteration on the accuracy was monitored.

4.4.2 Temporal term

The construction of the temporal term started similar to the spatial term. $P(nf)$ was converted to a F/NF classification. A neighborhood was used as well. However, the temporal neighborhood looked back in time for the PoI. At the current time (t) the converted $P(nf)$ was used, but at previous time-steps ($t - x$) the classification output of the MRF was used.

The sum of NF pixels in the temporal neighborhood including time t (2 pixels), was divided by the total number of pixels in the neighborhood (3 pixels), see Figure 4.6.

For the T-MRF, the number of time-steps (x) was varied between 1, 2 and 3 for which the results were studied. For $x = 2$ and $x = 3$, the temporal term was calculated as stated above. However, for $x = 1$ a Land Cover Trajectory (LCT) approach with a transition matrix was used. The LCT determined which LULC classes were more likely or less likely to change, because a deforested area is likely to still be deforested in the next image since trees recover slowly. These land cover trajectories were modeled with a transition matrix (Table 4.1). This transition matrix allows for all changes

to be possible, with the exception of a F pixel changing into a NF pixel.

The T-MRF was executed on the time-series in chronological order. Computation at time t relies on previously computed output at time $t - x$. For the first couple of time-steps (x) in the time-series, the RF output & threshold classification ($\theta = 0.5$) was used.

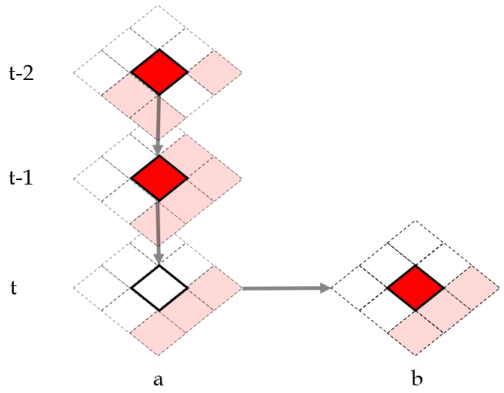

FIGURE 4.6: Visual representation of the temporal term, where the classifications of the PoI are compared from t to $t - 2$. As 2 out of 3 time-steps were NF, the PoI at t is also converted to NF.

TABLE 4.1: Transition Matrix

		t	
		Non-Forest (NF)	Forest (F)
t-1	Non-Forest (NF)	0	1
	Forest (F)	0	0

4.4.3 Space-Time MRF

In the ST-MRF, the unary, spatial and temporal terms were combined. The results of the T-MRF were used to determine the number of time-steps (x) to use for the temporal term in the ST-MRF. And the results from the S-MRF were used to determine the number of iterations to use in the ST-MRF.

Like the T-MRF, the ST-MRF was applied on the time-series chronologically, using the previous time-steps output as input. Therefore, ST-MRF could also not be applied at the start of the time-series. Instead, only the S-MRF was used for x time-steps.

4.5 Deforestation rate Riau

For determining the deforestation in Riau, the best MRF solution was used. The observation period start in 2014 and ended in 2017. Therefore, only the years 2015 and 2016 were entirely covered. The deforestation rate was therefore only determined

for 2015 and 2016. The forest mask of Figure 3.3 was used to mask data other than forests.

4.6 Validation

In order to validate the MRF, multiple accuracy measures were used which can be divided in spatial and temporal accuracy measures. A confusion matrix was used, from which Overall Accuracy (OA), Producer's Accuracy (PA) and User's Accuracy (UA) were derived as the spatial accuracy measures. To determine the temporal accuracy, the mean time-lag (MTL) was used.

Next to temporal and spatial accuracy measures, the computation time was taken into consideration. Computation costs increase significantly when the MRF would be applied on larger areas, or as the number of iterations are increased. Therefore, the computation costs were monitored for all components, tracking the elapsed time for computing each image. The computations were executed on a machine with 7.80 GB usable RAM and a processing speed of 2.59 GHz with 4 cores.

4.6.1 Spatial accuracy

Table 4.2 shows the confusion matrix (Hay, 1988) for the two classes used in this thesis. Using Equation 4.4, OA was derived. OA is the ratio of the correctly classified pixels of the total amount. The PA, 1 - Commission Error (% undetected events, Equation 4.5), is a measure of the pixels that are correctly included in the NF category. The UA, 1 - Omission Error (% false detections, Equation 4.6) is a measure of the pixels that are correctly excluded in the NF category. For example, a UA of 60% means that 60% of the data was correctly excluded of the NF class, and 40% was incorrectly included in the NF class. All three accuracy measures were estimated with the validation data gathered with the sampling scheme described in Section 4.2. The PA and UA, were only estimated for the NF class. The OA was estimated with NF and F data, thus giving an overall estimation of the classification accuracy instead of a focus on the NF class.

TABLE 4.2: Confusion Matrix

		Predicted	
		NF	F
Actual	NF	True Positive (TP)	False Negative (FN)
	F	False Positive (FP)	True Negative (TN)

$$OA = \frac{TP + TN}{TP + TN + FP + FN} \tag{4.4}$$

$$CE = \frac{FN}{FN + TP} \tag{4.5}$$

$$OE = \frac{FP}{FP + TP} \tag{4.6}$$

4.6.2 Temporal accuracy

The mean time-lag (MTL) was used for determining the temporal accuracy, following Reiche et al. (2015a) and Reiche et al. (2018). The MTL is the mean difference between the detection date and the reference date in days. The reference date was defined as the first date at which the deforestation event was visible in the time-series. And the detection date was the date at which the model first detected the deforestation event, see Figure 4.7.

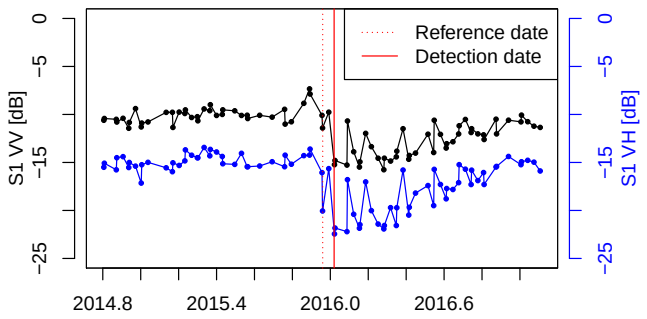

FIGURE 4.7: An example of the difference between the reference date and the detection date.

5 Results

The S-MRF with low spatial weight, $\lambda_{spatial} = 0.1$, showed little movement on any accuracy measure (Figure 5.1). After a maximum of 3 iterations, a stable situation was reached, and iterations were halted. As $\lambda_{spatial}$ increased, the maximum number of iterations increased as well. Simultaneously, the accuracy measures showed larger improvements, except for the PA, which decreased slightly as $\lambda_{spatial}$ and the number of iterations increased. The MTL showed an increase after iteration 8 with $\lambda_{spatial} = 0.9$.

In both the temporal and the spatial accuracies, the rate of improvement was largest for the first 3 iterations. Hereafter, the rate of improvement decreased while computation time increased consistently (Figure 5.3). Figure 5.2 shows a visual example of the iterations with $\lambda_{unary} = 0.1$ and $\lambda_{spatial} = 0.9$. Here, it is clearly visible that fragmented areas were removed, while the main deforestation area was maintained. At last, the first 3 iterations show more improvements compared to the use of more iterations.

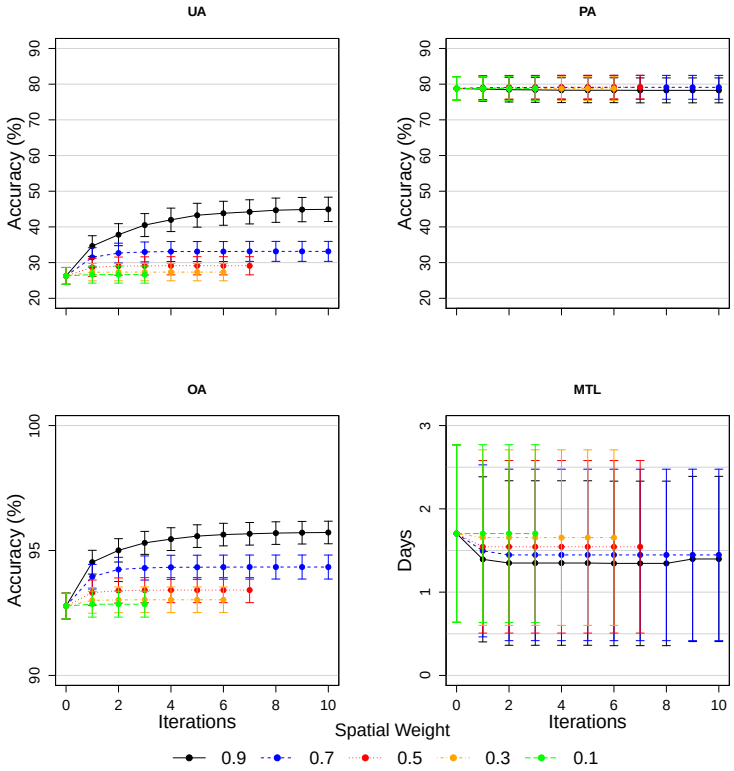

FIGURE 5.1: Spatial accuracy (PA and UA = producer's and user's accuracies of the deforestation class; OA = overall accuracy), and temporal accuracy (MTL = mean time lag of detected deforestation events) as a function of increasing number of iterations, with iteration 0 being the results before application of the MRF.

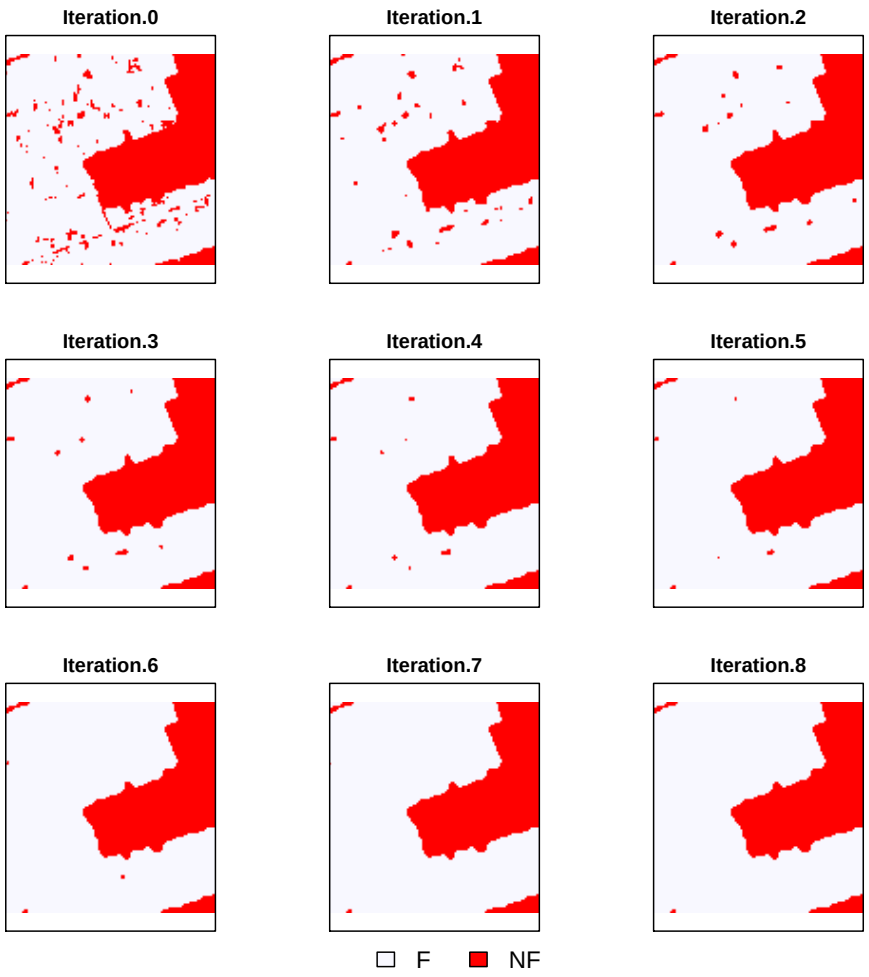

FIGURE 5.2: A visual example of the effect of iterations on the classification ($\lambda_{unary} = 0.1$ and $\lambda_{spatial} = 0.9$). Iteration 0 is the result before application of the MRF.

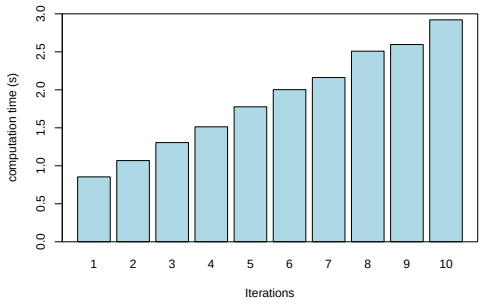

FIGURE 5.3: Average computation time per image, for the number of iterations of the MRF process.

The T-MRF's which had a low temporal weight, $\lambda_{temporal} <= 0.3$, showed only minor change. Difference become visible when the $\lambda_{temporal}$ was increased (Figure 5.4).

When $\lambda_{temporal}$ increased for $x = 1$, the UA, OA and MTL decreased, while the PA increased. In Figure 5.5 (left) is shown that a large number of pixels were classified as NF. Differing $\lambda_{temporal}$ between 0.5 and 0.9 had minor effects on the results.
There were visible effects for $x = 2$, as $\lambda_{temporal}$ increased. The UA, OA and MTL would increase, while PA decreased. With the highest UA and OA being with $\lambda_{temporal} = 0.7$, see this result in Figure 5.5 (middle). When $\lambda_{temporal}$ was increased to 0.9, the UA, PA decreased severely to 8% and the MTL decreased to 0 days.
When $x = 3$, the results showed similar behavior as $x = 2$. However the severe decrease which occurred at $\lambda_{temporal} = 0.9$ for $x = 2$, occurred for $x = 3$ at $\lambda_{temporal} >= 0.7$. Here, few pixels were classified as NF, as is shown in Figure 5.5 (right). The computation times in Figure 5.6 increased as x increased.

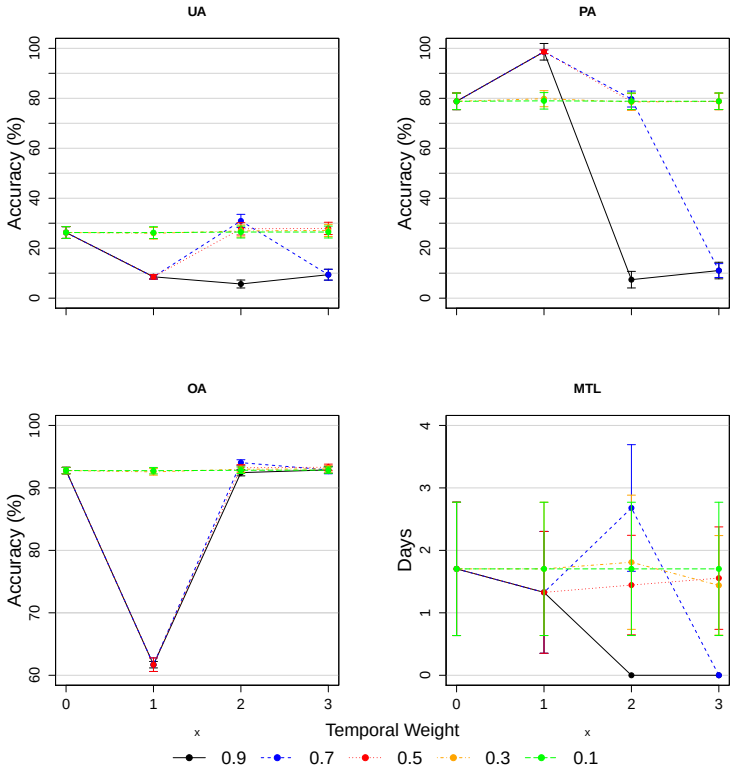

FIGURE 5.4: Spatial accuracy (PA and UA = producer's and user's accuracies of the deforestation class; OA = overall accuracy), and temporal accuracy (MTL = mean time lag of detected deforestation events) as a function of x for different weight distributions, with $x = 0$ being the results before application of the MRF.

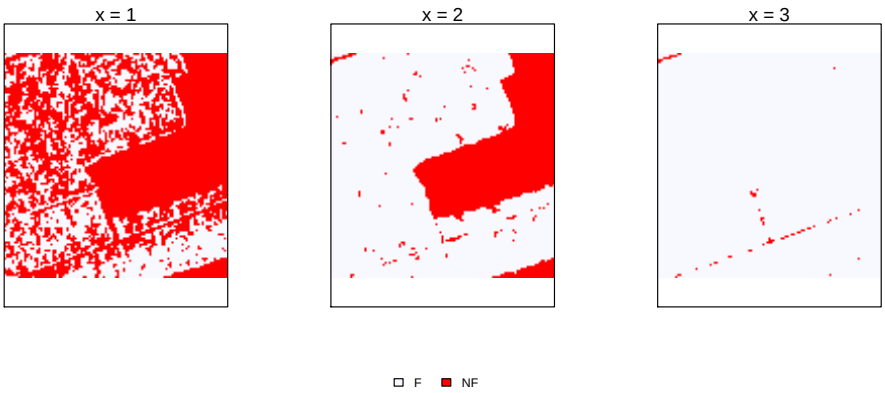

FIGURE 5.5: A visual example of the effect of the neighborhood size on the classification ($\lambda_{unary} = 0.3$ and $\lambda_{temporal} = 0.7$).

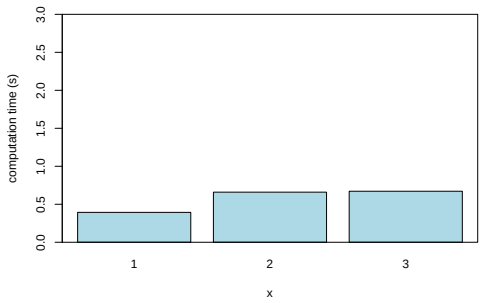

FIGURE 5.6: Average computation time per image for the different x.

For the ST-MRF, x was set to 2 as it showed the largest improvement in UA with minor decrease in MTL. The maximum number of iterations was set to 3 in order to keep computation costs low. The results are shown in triangle plots in Figure 5.7. Here, the points with high $\lambda_{temporal}$, have a low spatial and temporal accuracy like the T-MRF.

In order to elaborate the results, two cases have been highlighted. Case 1 ($+$) with $\lambda_{unary} = 0.6$, $\lambda_{spatial} = 0.2$ and $\lambda_{temporal} = 0.2$, had a low spatial accuracy with UA, PA and OA being 27%, 79% and 93% respectively. The temporal accuracy is high for the first case with a MTL of 2 days.

Case 2 ($\times$) with $\lambda_{unary} = 0.1$, $\lambda_{spatial} = 0.2$ and $\lambda_{temporal} = 0.7$, had an increased performance on the UA and OA, which were 54% and 97% respectively. But the PA decreased to 68% and the MTL increased to 11 days.

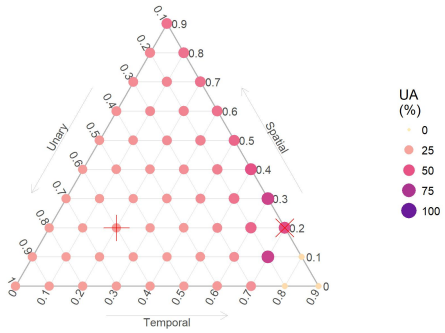

(A) User's Accuracy

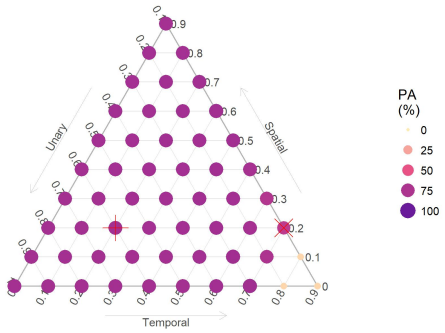

(B) Producer's Accuracy

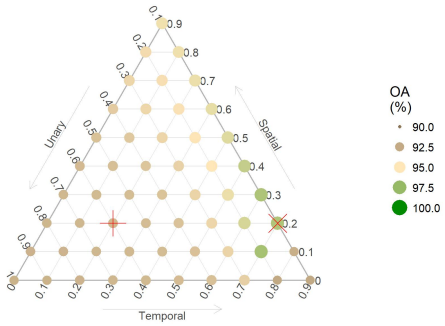

(C) Overall Accuracy

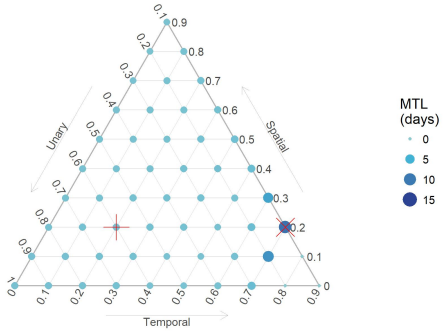

(D) Mean time-lag

FIGURE 5.7: Spatial and temporal accuracy measures in triangle plots. Each combination of weights ($\lambda_{unary} + \lambda_{spatial} + \lambda_{temporal} = 1$) is represented by a point. two cases have been highlighted (case 1: $+$ and case 2: $\times$)

In Figure 5.8 an example of the different MRF's is shown with the corresponding input images. All three MRF approaches (bottom) show improvement compared to the image before MRF execution (top-middle). The S-MRF (bottom-left) shows scattered deforestations outside the main area. The scattered deforestation were less dominantly present in the T-MRF (bottom-middle), to finally disappear in the ST-MRF (bottom-right). In addition, the borders of the deforested areas were more accurately maintained in the ST-MRF.

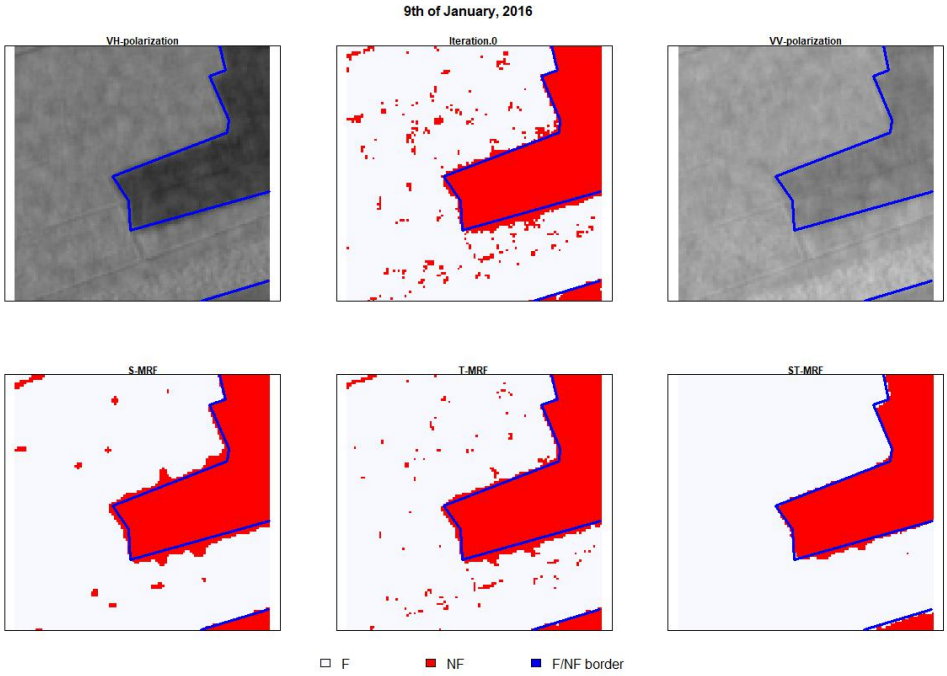

FIGURE 5.8: Results of the different MRF's after 3 iterations: S-MRF ($\lambda_{unary} = 0.1$, $\lambda_{spatial} = 0.9$), T-MRF ($\lambda_{unary} = 0.3$, $\lambda_{temporal} = 0.7$) and ST-MRF ($\lambda_{unary} = 0.2$, $\lambda_{spatial} = 0.1$, $\lambda_{temporal} = 0.7$) with the used input (VV & VH). The border of the deforested areas are highlighted in blue, where VV & VH have been used as the ground-truth.

The deforestation rate of Riau was determined quarterly for the observation period (Figure 5.9a). For the years 2015 and 2016, the deforestation rate was 7.1% and 7.4% respectively. Because the temporal scale (three months) was much larger compared to the revisit time of Sentinel-1 (10 days), the temporal accuracy was not as important as the spatial accuracy. Therefore the weight distribution of $\lambda_{unary} = 0.1$, $\lambda_{spatial} = 0.2$ and $\lambda_{temporal} = 0.7$ was used.

Large homogeneous deforested areas were distinguished (Figure 5.9a). Throughout the study area, single pixels and small areas have also been detected (Figure 5.9b and 5.8). This is mostly visible in areas where the forest was fragmented and at the edges of the forest mask.

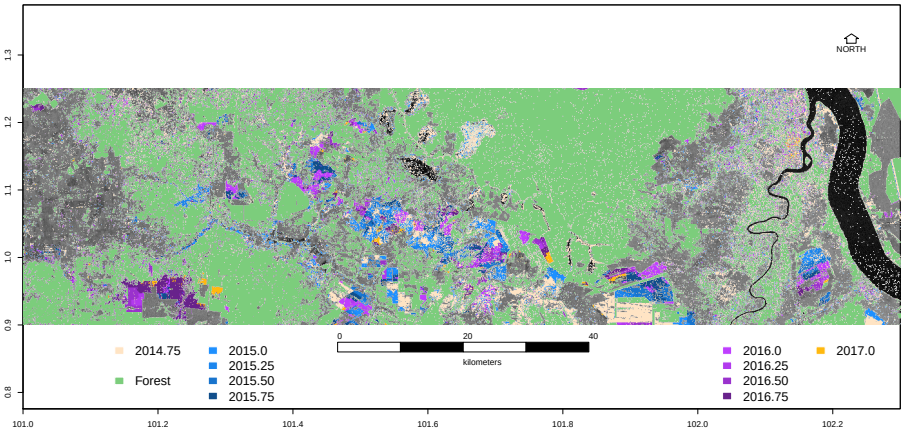

(A)

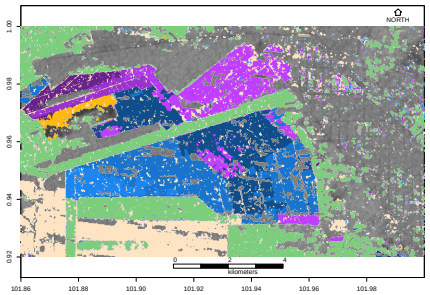

(B)

FIGURE 5.9: The detected deforestation during the observation period, grouped quarterly. For (A) the study area in Riau and (B) a zoomed in part of the study area. The background shows the VH-polarization acquisition at the end of the time-series.

6 Discussion

Adapting a MRF for time-series deforestation detection in tropical regions has shown that it generally improves results. The proposed approach of using a space-time MRF is generally able to capture deforestation events. The results showed that the use of the proposed approaches outperform a standard RF classification, in terms of classification accuracy. Additional testing showed that the T-MRF, despite generally being not as effective as the S-MRF, can be used to significantly increase accuracies. These findings are in agreement with the results of other recent studies, which were able to improve the classification accuracy by implementation of multi-temporal MRF (Wehmann and Liu, 2015; Liu et al., 2008; Hagensieker et al., 2017).

Iteration 0 was the result of applying $\theta = 0.5$ to $P(nf)$. And $P(nf)$ was the result of a RF model. Iteration 0 had a low UA and slightly higher PA (Figure 5.1), because it has wrongly included many pixels in the NF class. This is also visible in Figure 5.2. It was up to the MRF to put those wrongly classified pixels back in the F class, in other words: to increase UA. The S-MRF performed well in this regard, especially with higher $\lambda_{spatial}$. The increase in $\lambda_{spatial}$ forced the MRF to depend more on the neighborhood, instead of $P(nf)$. As a result, NF pixels without a majority of F neighbors were converted to F. This process continued with the increase of iterations, so not only single pixels were converted, but the areas as well. However, some pixels were wrongly classified as F during this process, because the PA decreased slightly.

The MTL in Figure 5.1 stabilized after 2 iterations for $\lambda_{spatial} = 0.9$, and started to increase again after 8 iterations. At the start of the iteration process, the MRF improves the results, converting pixels based on their neighborhood. However, the MRF does not know when to stop, because of an assumption of the ICM. The ICM assumes that the best possible solution will be when there are no changes detected between iterations. Thus it continued to change areas from NF to F, whether it was correct or incorrect.
Correctly classified NF pixels, were converted to F as the number of iterations increased. Thus the date of detection was delayed to a date where the $P(nf)$ was high enough to counter the spatial neighborhood. This resulted in an increase of the MTL.

In order to counter this, it was desirable to manually set a maximum number of iteration, instead of letting it run until no changes occur anymore. This is also recommendable when the computation time is considered, confirming the findings of Solberg, Taxt, and Jain (1996) and Besag (1986). For the S-MRF with low $\lambda_{spatial}$ the ICM did not need many iterations. However, as $\lambda_{spatial}$ increased the ICM would need more and more iterations, going into the hundreds for some images. Here, the model becomes more dependent on the spatial term. As the spatial terms becomes more important, changes are more likely to happen and therefore more iterations were needed. The ICM uses these iterations to reach a local optimum of the energy of the pixel. An approach like graph-cut (Szeliski et al., 2008) uses a global optimization technique. This could be beneficial by reaching a global optimum with less

computational cost than running ICM completely (Kohli, Ladický, and Torr, 2009). However, the initial computation costs of a graph-cut could be higher than limiting the ICM's iterations (Vineet and Narayanan, 2008).

The T-MRF with $x = 1$ used a transition matrix, which specified that only a transition from NF to F would be penalized by 1. The effect was that pixels classified as NF would have difficulty transitioning back to F, including all the erroneous classifications (Figure 5.5). These errors could not be corrected by the $P(nf)$ when $\lambda_{temporal} >= 0.5$. Therefore the number of errors increased with each time-step. Thus many pixels were classified as NF, correctly and incorrectly, resulting in a high PA and low UA. More research on the transition matrix could benefit the T-MRF, as this approach had the lowest computation costs (Figure 5.6).

For $x = 3$, $\lambda_{temporal} >= 0.7$ showed different behavior than the other weight distributions. Here, many pixels were classified as F instead of NF. The model became very dependent on the history of a pixel before the deforestation event, and therefore preferred F over NF. The next time-step would use this wrongly classified pixel for the classification. The error therefore propagated through the time-series and many deforestation events were not detected (Figure 5.5).

The process described above also occurred for $x = 2$ with $\lambda_{temporal} = 0.9$. It occurred at a higher weight as it used less neighbors to estimate the class at time t. Having less neighbors suggesting the F class influence the energy in the temporal neighborhood term, as a neighborhood of 3 pixels allows for lower values compared to a neighborhood of 4 pixels, e.g. $3/4$ versus $2/3$.

The T-MRF showed differences in OA. The OA decreased to 63% with $x = 1$ while the $x > 1$ was around 93%. The OA used both F and NF classes, and the NF samples in the validation were outnumbered by the F samples. Therefore $x = 1$ shows a decrease in OA, as many F pixels were wrongly classified. In contrast to $x > 1$, where the OA remained high. Here, the wrongly classified NF pixels were few compared to the many correctly classified F pixels.

In Figure 5.7 two cases were highlighted. If the figures are compared with each other, the following principle can be derived: as the UA and OA increases, the PA and MTL decreases. This makes it nearly impossible to point out the "best" approach. The best approach will depend on the case of the user, either demanding a high spatial accuracy ($\times$), a high temporal accuracy ($+$) or a medium spatial and temporal accuracy. This trade-off has also been found by other studies (Reiche et al., 2018; Zhu, Woodcock, and Olofsson, 2012; Reiche et al., 2015b; Hamunyela et al., 2016).

The forest mask used for Figure 5.9 was developed for global estimation of tree and vegetation cover. Some errors arise by using it on a smaller scale e.g. homogeneous areas appear noisy despite texture features that were included in the classification procedure. The results were affected by typical SAR-inherent noise, so-called speckle. The used forest mask was also derived from satellite imagery, and therefore also susceptible to errors (Hansen et al., 2008). Small fragmented areas could have been suppressed as the MRF includes spatial context. Especially when the ground resolution is coarse relative to the size of the deforestation event.

The greediness of the RF model was due to the selection of the training data. The RF was trained with the data collected at the reference date, see Figure 4.7. The data of F was distributed around -15 dB. For NF, the distribution decreased to around -20 dB. The reference date was usually placed at the start of or in a transition period. The values collected at the reference date were closer to -15 dB instead of -20 dB, and thus more likely to overlap with the distribution of F. This made it difficult for the RF model to separate the classes. Due to the focus on MRF capabilities in this study, the class separability was not improved.

The MTL was determined from the reference date, the first acquisition showing the deforestation event. In reality however, the deforestation happened in between the reference date and the previous acquisition. This was also stated by Reiche et al. (2018), where the reference date was adjusted. However the exact date of deforestation remains unknown. To be able to detect more closely to the actual event, an increase in SAR acquisition density is needed. Therefore, other SAR satellites could be included in the classification scheme, following methods presented by Reiche et al. (2015b), Asner (2009), Hansen et al. (2008), and Reiche et al. (2015a).

7 Conclusion

The MRF generally improved deforestation detection in time-series, where a spatial and temporal combination showed the most potential. By increasing the number of iterations, the spatial and temporal accuracies could be further improved. However, the increase in computation costs have to be considered. The computation costs could be reduced by using a transition matrix, only using $t - 1$. But the transition matrix has to adjusted, as it did not result in improved classification results in this study. The S-MRF outperformed the T-MRF. When combined however, the temporal term showed to be highly important for the spatial accuracy. The ST-MRF has shown to be a powerful tool in improving deforestation detection in time-series. Currently, the ST-MRF uses a local optimization technique, the ICM. An optimization technique like graph-cut (Szeliski et al., 2008) would allow for a global optimum.

A Appendix

This was developed in Rstudio v3.3.2. with the following package distributions:

- rgdal 1.2-18
- raster 2.6-7
- randomForest 4.6-14
- sp 1.2.7

Below is an example code used for the ST-MRF. Data and code are available via https://git.wageningenur.nl/ent004/MscThesis_ST-MRF.

```
require(rgdal)
require(raster)
require(randomForest)
require(sp)

## import functions
source("functions/not.in.R")
source("functions/ST.MRF.R")


## set maximum iterations
maximum_iterations <- 3
## set threshold for NF probability for classification
NF.threshold <- 0.5
## load modelRF
load(file = "data/RFmodel")


## Set weights: c(unary, spatial, temporal)
## with unary > 0 & unary + spatial + temporal = 1
ws <- c(0.1,0.1, 0.8)



## load S1 DATA of Study Area
s1vv_stack <- stack("data/StudyArea_S1VV.grd")
s1vh_stack <- stack("data/StudyArea_S1VH.grd")

plot.image <- 42
### Plot s1vv and s1vh images
```

```
par(mfrow=c(1,2))
## create greyscale
greyscale <- grey.colors(300, start = 0, end = 1, alpha = NULL, gamma = 1)
plot(s1vv_stack, plot.image, zlim = c(-30,0), col = greyscale,
        main = "S1VV")
plot(s1vh_stack, plot.image, zlim = c(-30,0), legend = F,
        col = greyscale, main = "S1VH")
par(mfrow=c(1,1))


### Run MRF by looping through all images in the s1vh stack
for (imagenr in 1:nlayers(s1vh_stack)){
        ## subset single image
        s1vv.single <- subset(s1vv_stack, imagenr)
        s1vh.single <- subset(s1vh_stack, imagenr)
        ## combine in brick, and changes names to match with modelRF
        data_brick <- brick(s1vv.single, s1vh.single)
        names(data_brick) <- c("s1vv", "s1vh")
        ## make PNF
        predLC <- raster::predict(data_brick, model=modelRF,
                na.rm=TRUE, type = "prob")
        PNF <- 1-predLC
        # plot(PNF)

        ## Convert PNF to strict classes
        class <- cut(x=PNF, breaks = c(-0.1,NF.threshold,1.1))
        # plot(class)

        ## initialze iterative loop
        continue <- T
        iteration <- 1
        while (continue){

                ## Temporal MRF check and pre-proces
                if ((ws[3] != 0) & (imagenr %!in% 1:2)){
                ## do not perform temporal MRF on first image
                        ## load previous timestep
                        prev_MRF1 <- brick(paste0("ST-MRF/img",
                                (imagenr-1),".grd"))
                        prev_MRF2 <- brick(paste0("ST-MRF/img",
                                (imagenr-2),".grd"))


                        ## calculate normalized nb of temporal neighbors
                        temp.rel <- overlay(x=class,
                                y = prev_MRF1[[nlayers(prev_MRF1)]],
                                z = rev_MRF2[[nlayers(prev_MRF2)]],
                                fun = mean)
                        temp.rel <- temp.rel-1

                } else {
```

```
        temp.rel <- class
        ## Assign 0.5, because this wont make a difference
        ## in MRF (term vs 1-term)
        temp.rel[temp.rel$layer] <- 0.5
}

## Spatial check and pre-proces
if ((ws[2] != 0)){
        if (iteration == 1){
                spat.rel <- focal(class, w = matrix(1,3,3),
                        fun = function(matrix)
                        {mean(matrix)-1}, pad=T,
                        padValue = 1.5)
        } else {
                spat.rel <- focal(mrf.brick[[iteration - 1]],
                        w = matrix(1,3,3),
                        fun = function(matrix)
                        {mean(matrix)-1}, pad=T,
                        padValue = 1.5)
        }
} else{
        spat.rel <- class
        ## Assign 0.5, because this wont make a difference
        ## in MRF (term vs 1-term)
        spat.rel[spat.rel$layer] <- 0.5

        ## force no iterations
        continue <- F
}

## Check both T&S
if ((ws[2] != 0) | (ws[3] != 0)){
        ## Perform MRF
        mrf.output <- overlay(x = PNF, y = spat.rel,
                temporal = temp.rel, fun = ST.mrf)
        ## add one to number it iteration
} else { # skip MRF
        mrf.output <- class
}
names(mrf.output) <- paste0("IMG_",imagenr)

if (iteration > 1){
        ## check if the new one is equal to last,
        ## stop procedure if equal
        if ((all.equal(mrf.output,
                mrf.brick[[nlayers(mrf.brick)]])) |
                (iteration > (maximum_iterations))) {
                continue <- F
        } else { ## add to mrf.brick
                mrf.brick <- addLayer(mrf.brick, mrf.output)
        }
```

```
                } else {
                        mrf.brick <- mrf.output
                }
                iteration <- iteration + 1
        }

        ## create new folder, if necessary
        if (!dir.exists(file.path(paste0(getwd(),"/ST-MRF")))){
                dir.create("ST-MRF")}
        ## Save output with IMAGENR tag
        writeRaster(mrf.brick, filename = paste0("ST-MRF/img",imagenr,
                ".grd"), overwrite = T)
}

## combine final iterations into 1 brick
Final.MRFs <- brick()
for (imagenr in 1:nlayers(s1vh_stack)){
        image.file <- brick(paste0("ST-MRF/img",imagenr,".grd"))
        Final.MRFs <- addLayer(Final.MRFs,
                image.file[[nlayers(image.file)]])
}
writeRaster(Final.MRFs, filename = paste0("Final.MRFs.grd"),
        overwrite = T)

#### Plot an image ####
plot.image <- 42
if (Final.MRFs[[plot.image]]@data@max == 2){
        plot(Final.MRFs[[plot.image]], col=c("ghostwhite", "red"),
                legend = F, axes = T, main = "")
} else {
        plot(Final.MRFs[[plot.image]], col="ghostwhite",
                legend = F, axes = T, main = "")
}
legend("topright", c("Forest", "Non-Forest"), xpd = TRUE, horiz = F,
        inset = c(-0.20,0), fill = c("ghostwhite", "red"))
```

Bibliography

Achard, F. (2002). "Determination of Deforestation Rates of the World's Humid Tropical Forests". In: *Science* 297, pp. 999–1002.

Almeida-Filho, R. et al. (2009). "Using dual polarized ALOS PALSAR data for detecting new fronts of deforestation in the Brazilian Amazônia". In: *International Journal of Remote Sensing* 30.14, pp. 3735–3743.

Asner, G.P. (2009). "Tropical forest carbon assessment: Integrating satellite and airborne mapping approaches". In: *Environmental Research Letters* 4.3.

Assunção, J., C. Gandour, and R. Rocha (2013). "DETERring Deforestation in the Brazilian Amazon: Environmental Monitoring and Law Enforcement". In: *Climate Policy Initiative*, pp. 1–36.

Belgiu, M. and L. Drăgu (2016). "Random forest in remote sensing: A review of applications and future directions". In: *ISPRS Journal of Photogrammetry and Remote Sensing* 114, pp. 24–31.

Bengio, Y., A. Courville, and P. Vincent (2013). "Representation learning: A review and new perspectives". In: *IEEE Transactions on Pattern Analysis and Machine Intelligence* 35.8, pp. 1798–1828.

Besag, J. (1986). "On the Statistical Analysis of Dirty Pictures". In: *Journal of the Royal Statistical Society* 48.3, pp. 259–302.

Blaes, X., L. Vanhalle, and P. Defourny (2005). "Efficiency of crop identification based on optical and SAR image time series". In: *Remote Sensing of Environment* 96.3-4, pp. 352–365.

Brack, D. (2003). "Illegal logging and the illegal trade in forest and timber products". In: *International Forestry Review* 5.3, pp. 195–198.

Breiman, L. (2001). "Random forests". In: *Machine Learning* 45.1, pp. 5–32.

Cai, S. et al. (2014). "Enhancing MODIS land cover product with a spatial-temporal modeling algorithm". In: *Remote Sensing of Environment* 147, pp. 243–255.

Cohen, W.B., Z. Yang, and R. Kennedy (2010). "Detecting trends in forest disturbance and recovery using yearly Landsat time series: 2. TimeSync - Tools for calibration and validation". In: *Remote Sensing of Environment* 114.12, pp. 2911–2924.

Cohen, W.B. et al. (1996). "An introduction to digital methods in remote-sensing of forested ecosystems - focus on the Pacific-Northwest, USA". In: *Environmental Management* 20.3, pp. 421–435.

Coppin, P. et al. (2004). "Digital change detection methods in ecosystem monitoring: A review". In: *International Journal of Remote Sensing* 25.9, pp. 1565–1596.

Coulston, J.W. et al. (2012). "Modeling percent tree canopy cover—a pilot study". In: *Photogrammetric Engineering and Remote Sensing* 78.7, pp. 715–727.

Du, P. et al. (2015). "Random Forest and Rotation Forest for fully polarized SAR image classification using polarimetric and spatial features". In: *ISPRS Journal of Photogrammetry and Remote Sensing* 105, pp. 38–53.

Foley, J.A. (2005). "Global Consequences of Land Use". In: *Science* 309.5734, pp. 570–574.

Fu, W., Z. Guo, and Q. Zhou (2009). "A spatial-temporal contextual classification approach based on Markov random fields using multi-temporal imagery". In: *Sixth*

International Symposium on Multispectral Image Processing and Pattern Recognition. Vol. 7496, p. 74961I.

Fuller, D.O. (2006). "Tropical forest monitoring and remote sensing: A new era of transparency in forest governance?" In: *Singapore Journal of Tropical Geography* 27.1, pp. 15–29.

Gislason, P.O., J.A. Benediktsson, and J.R. Sveinsson (2006). "Random forests for land cover classification". In: *Pattern Recognition Letters* 27.4, pp. 294–300.

Goodman, J. W. (1976). "Some fundamental properties of speckle". In: *Journal of the Optical Society of America* 66.11, pp. 1145–1150.

Hagensieker, R. et al. (2017). "Tropical land use land cover mapping in Pará (Brazil) using discriminative Markov random fields and multi-temporal TerraSAR-X data". In: *International Journal of Applied Earth Observation and Geoinformation* 63, pp. 244–256.

Hamunyela, E. et al. (2016). "Monitoring deforestation at sub-annual scales as extreme events in landsat data cubes". In: *Remote Sensing* 8.651.

Hansen, M.C. et al. (2008). "A method for integrating MODIS and Landsat data for systematic monitoring of forest cover and change in the Congo Basin". In: *Remote Sensing of Environment* 112.5, pp. 2495–2513.

Hansen, M.C. et al. (2013). "High-Resolution Global Maps of 21st-Century Forest Cover Change". In: *Science* 342, pp. 850–854.

Hay, A.M. (1988). "Remote sensing letters the derivation of global estimates from a confusion matrix". In: *International Journal of Remote Sensing* 9.8, pp. 1395–1398.

Holloway, V. and E. Giandomenico (2009). *The History of REDD Policy*. Tech. rep. December, p. 20.

Joshi, N. et al. (2015). "Mapping dynamics of deforestation and forest degradation in tropical forests using radar satellite data". In: *Environmental Research Letters* 10.3, pp. 1–13.

Kasischke, E.S., J.M. Melack, and M.C. Dobson (1997). "The use of imaging radars for ecological applications—A review". In: *Remote Sensing of Environment* 59.2, pp. 141–156.

Kohli, P., L. Ladický, and P.H.S. Torr (2009). "Robust higher order potentials for enforcing label consistency". In: *International Journal of Computer Vision* 82.3, pp. 302–324.

Kumar, T. and C. Patnaik (2013). "Discrimination of mangrove forests and characterization of adjoining land cover classes using temporal C-band Synthetic Aperture Radar data: A case study of Sundarbans". In: *International Journal of Applied Earth Observation and Geoinformation* 23.1, pp. 119–131.

Li, R. et al. (2008). "Long-term effects of eliminating illegal logging on the world forest industries, trade, and inventory". In: *Forest Policy and Economics* 10.7-8, pp. 480–490.

Li, W. et al. (2011). "Tropical forest mapping and change detection using ALOS PALSAR data". In: *International Symposium on Lidar and Radar Mapping 2011: Technologies and Applications*.

Liaw, A. and M. Wiener (2002). "Classification and Regression by randomForest". In: *R news* 2.3, pp. 18–22.

Liu, D. and S. Cai (2012). "A Spatial-Temporal Modeling Approach to Reconstructing Land-Cover Change Trajectories from Multi-temporal Satellite Imagery". In: *Annals of the Association of American Geographers* 102.6, pp. 1329–1347.

Liu, D., M. Kelly, and P. Gong (2006). "A spatial-temporal approach to monitoring forest disease spread using multi-temporal high spatial resolution imagery". In: *Remote Sensing of Environment* 101.2, pp. 167–180.

Liu, D. et al. (2008). "Using local transition probability models in Markov random fields for forest change detection". In: *Remote Sensing of Environment* 112.5, pp. 2222–2231.

Lu, D. and Q. Weng (2007). "A survey of image classification methods and techniques for improving classification performance". In: *International Journal of Remote Sensing* 28.5, pp. 823–870.

Lu, D. et al. (2004). "Change detection techniques". In: *International Journal of Remote Sensing* 25.12, pp. 2365–2407.

Lynch, J. et al. (2013). "Choose satellites to monitor deforestation". In: *Nature* 496, pp. 293–294.

McNairn, H. et al. (2009). "Integration of optical and Synthetic Aperture Radar (SAR) imagery for delivering operational annual crop inventories". In: *ISPRS Journal of Photogrammetry and Remote Sensing* 64.5, pp. 434–449.

Melgani, F. and S.B. Serpico (2003). "A Markov Random Field Approach to Spatio-Temporal Contextual Image Classification". In: *IEEE Transactions on Geoscience and Remote Sensing* 41.11, pp. 2478–2487.

Mermoz, S. and T. Le Toan (2016). "Forest disturbances and regrowth assessment using ALOS PALSAR data from 2007 to 2010 in Vietnam, Cambodia and Lao PDR". In: *Remote Sensing* 8.3, pp. 1–22.

Moser, G. and S.B. Serpico (2013). "Combining support vector machines and Markov random fields in an integrated framework for contextual image classification". In: *IEEE Transactions on Geoscience and Remote Sensing* 51.5, pp. 2734–2752.

Moser, G., S.B. Serpico, and J.A. Benediktsson (2013). "Land-cover mapping by markov modeling of spatial-contextual information in very-high-resolution remote sensing images". In: *Proceedings of the IEEE*. Vol. 101. 3, pp. 631–651.

Müller, H. et al. (2015). "Mining dense Landsat time series for separating cropland and pasture in a heterogeneous Brazilian savanna landscape". In: *Remote Sensing of Environment* 156, pp. 490–499.

Myers, N. (1988). "Tropical deforestation and climatic change." In: *Environmental Conservation* 15.4, pp. 293–298.

Qi, Z. et al. (2012). "A novel algorithm for land use and land cover classification using RADARSAT-2 polarimetric SAR data". In: *Remote Sensing of Environment* 118, pp. 21–39.

Rahman, M.M. and J.T.S. Sumantyo (2010). "Mapping tropical forest cover and deforestation using synthetic aperture radar (SAR) images". In: *Applied Geomatics* 2.3, pp. 113–121.

Reiche, J. et al. (2013). "Feature Level Fusion of Multi-Temporal ALOS PALSAR and Landsat Data for Mapping and Monitoring of Tropical Deforestation and Forest Degradation". In: *IEEE Journal of Selected Topics in Applied Earth Observations and Remote Sensing* 6.3, pp. 2159–2173.

Reiche, J. et al. (2015a). "A Bayesian approach to combine landsat and ALOS PALSAR time series for near real-time deforestation detection". In: *Remote Sensing* 7.5, pp. 4973–4996.

Reiche, J. et al. (2015b). "Fusing Landsat and SAR time series to detect deforestation in the tropics". In: *Remote Sensing of Environment* 156, pp. 276–293.

Reiche, J. et al. (2016). "Combining satellite data for better tropical forest monitoring". In: *Nature Climate Change* 6.2, pp. 120–122.

Reiche, J. et al. (2018). "Improving near-real time deforestation monitoring in tropical dry forests by combining dense Sentinel-1 time series with Landsat and ALOS-2 PALSAR-2". In: *Remote Sensing of Environment* 204, pp. 147–161.

Rufin, P. et al. (2015). "Land use intensity trajectories on Amazonian pastures derived from Landsat time series". In: *International Journal of Applied Earth Observation and Geoinformation* 41, pp. 1–10.

Ryan, C.M. et al. (2012). "Quantifying small-scale deforestation and forest degradation in African woodlands using radar imagery". In: *Global Change Biology* 18, pp. 243–257.

Santilli, M. et al. (2005). "Tropical deforestation and the Kyoto protocol". In: *Climatic Change* 71.3, pp. 267–276.

Schindler, K. (2012). "An overview and comparison of smooth labeling methods for land-cover classification". In: *IEEE Transactions on Geoscience and Remote Sensing* 50.11, pp. 4534–4545.

Sheng, Y. and Z. Xia (1996). "A comprehensive evaluation of filters for radar speckle suppression". In: *IGARSS '96. 1996 International Geoscience and Remote Sensing Symposium*, pp. 1559–1561.

Solberg, A.H.S., T. Taxt, and A.K. Jain (1996). "A Markov Random Field Model for Classification of Multisource Satellite Imagery". In: *IEEE Transactions on Geoscience and Remote Sensing* 34.1, pp. 100 –113.

Szeliski, R. et al. (2008). "A Comparative Study of Energy Minimization Methods for Markov Random Fields with Smoothness-Based Priors". In: *IEEE Transactions on Pattern Analysis and Machine Intelligence* 30.6, pp. 1068–1080.

Tobler, W.R. (1970). "A Computer Movie Simulation Urban Growth in Detroit Region". In: *Economic Geography* 46, pp. 234–240.

Trier, Ø.D. and A.B. Salberg (2011). "Time-series analysis of satellite images for forest cover change monitoring in Tanzania". In: *1st EARSeL Workshop on Operational Remote Sensing in Forest Management*, pp. 1–12.

Turner, J.A. et al. (2008). "Economic incentives exist to support measures to reduce illegal logging". In: *International Forestry Review* 10.1, pp. 74–80.

Uhlmann, S. and S. Kiranyaz (2014). "Classification of dual- and single polarized SAR images by incorporating visual features". In: *ISPRS Journal of Photogrammetry and Remote Sensing* 90, pp. 10–22.

Verbesselt, J. et al. (2010). "Detecting trend and seasonal changes in satellite image time series". In: *Remote Sensing of Environment* 114.1, pp. 106–115.

Vineet, V. and P.J. Narayanan (2008). "CUBA cuts: Fast graph cuts on the GPU". In: *2008 IEEE Computer Society Conference on Computer Vision and Pattern Recognition Workshops, CVPR Workshops*.

Vitousek, P.M. et al. (1997). "Human Domination of Earth' s Ecosystems". In: *Science* 277.5325, pp. 494–499.

Vuolo, F. et al. (2013). "Estimation of leaf area index using DEIMOS-1 data: Application and transferability of a semi-empirical relationship between two agricultural areas". In: *Remote Sensing* 5.3, pp. 1274–1291.

Waske, B. and M. Braun (2009). "Classifier ensembles for land cover mapping using multitemporal SAR imagery". In: *ISPRS Journal of Photogrammetry and Remote Sensing* 64.5, pp. 450–457.

Wehmann, A. and D. Liu (2015). "A spatial-temporal contextual Markovian kernel method for multi-temporal land cover mapping". In: *ISPRS Journal of Photogrammetry and Remote Sensing* 107, pp. 77–89.

Zhu, Z., C.E. Woodcock, and P. Olofsson (2012). "Continuous monitoring of forest disturbance using all available Landsat imagery". In: *Remote Sensing of Environment* 122, pp. 75–91.